

Maximizing Infrared Transmission Contrast Upon Phase Transition of Thermally Grown Vanadium Dioxide Thin Films by Rapid Thermal Processing

*Ken Araki, Vishwa Krishna Rajan, and Liping Wang**

K. Araki, V. K. Rajan, L. Wang

School for Engineering of Matter, Transport and Energy, Arizona State University, 501 E Tyler Mall, Tempe, AZ, 85287, USA

E-mail: liping.wang@asu.edu

Funding: NSF Grant No. CBET-2212342

Keywords: Vanadium dioxide, thermal oxidation, thermal reduction, infrared transmission contrast, hysteresis width

Abstract: Pristine vanadium dioxide (VO_2), an insulator-to-metal transition (IMT) material, is grown via furnace oxidation followed by rapid thermal annealing with forming gas (5% H_2 / 95% N_2) which reduces surface over-oxides such as V_2O_5 formed during the oxidation. The evolutional IMT behaviors of the thermochromic film and vanadium oxide states over different reduction time are systematically studied with temperature-dependent infrared spectrometry, electrical resistivity, and X-ray diffraction measurements. After optimally reducing surface over-oxides to VO_2 , infrared transmission contrast upon phase transition is enhanced to 46% (at 9 μm wavelength) compared to 23% from fully oxidation without any reduction. Moreover, pristine VO_2 thin film obtained from thermal oxidation and optimal reduction processes exhibits sharp phase transition and narrow thermal hysteresis within 2~4°C in both infrared transmission and electrical resistivity, which are comparable to the VO_2 of best quality prepared by other sophisticated fabrication techniques. The thermally grown method presented here would facilitate the scalable fabrication of high-quality VO_2 thin films and tunable radiative coatings for high-performance thermal control applications.

1. Introduction

Tunable optical and infrared properties of radiative coatings are highly desired for self-adaptive solar thermal energy harvesting and radiative thermal control to the changing environment. Vanadium dioxide (VO_2) as one of the most popular thermochromic materials has attracted lots of attention in such applications due to its unique insulator-to-metal transition (IMT).^[1] Tunable VO_2 coatings using Fabry-Perot cavity can switch from high reflective insulating phase to highly emissive metallic phase with an increase in temperature for passive radiative thermal control.^[2-5] Other VO_2 coatings can be employed as a radiative cooler during night time while it can behave as a selective solar absorber at day time.^[6-8] Tunable bandpass filters, which have the ability to pass both narrowband and broadband mid-infrared light only at insulating phase, are also designed based on VO_2 phase transition.^[9, 10] Due to its transparency at insulating phase, studies have also demonstrated anti-reflection in mid-infrared region by depositing thin layer of VO_2 on epsilon near-zero substrates.^[11, 12] Such technique can be used as a thermal rectifier that allow large difference between forward and reverse heat flow upon the phase transition temperature using VO_2 on doped silicon, demonstrated in far-field regime^[13] and on sapphire demonstrated in near-field regime.^[14]

Established methods to fabricate VO_2 thin films include molecular beam epitaxy (MBE),^[15, 16] reactive sputtering,^[17-20] atomic layer deposition (ALD),^[21-23] pulsed laser deposition (PLD),^[24, 25] sol-gel,^[26] hydrothermal process,^[27, 28] and thermal oxidation^[29, 30]. However, some growth techniques that provide best quality of VO_2 suffer from sophisticated equipment, expensive operation, slow deposition rate, or highly selective lattice-matched substrates, which greatly hinders the scalability. Other cost-effective techniques in particular thermal oxidation bears compromised film quality due to surface over-oxidation with vanadium pentoxide (V_2O_5) in oxygen-rich atmosphere, which causes unwanted phonon absorption, curtaining the contrast in the infrared properties upon phase transition.^[31] It has been demonstrated that with longer oxidation time, XRD intensity of VO_2 decreases while V_2O_5 signal increases as the vanadium film is oxidized in the air at atmospheric pressure.^[32] With rapid thermal oxidation, formation of V_2O_5 can be minimized but it requires precise time control from several seconds to one minute.^[33] Oxidation at high temperatures without control in oxygen partial pressure could result in high ratio of V_2O_5 .^[34] However, with precisely-controlled oxygen and hydrogen

concentrations, pristine VO₂ can be obtained as a result of a balance between over-oxidation and reduction.^[35] High quality VO₂ can be synthesized directly from further oxidizing V₂O₃ in well-controlled oxygen partial pressure.^[36] On the other hand, VO₂ can also be obtained from reducing ALD prepared high-oxides (V_xO_y with y/x >2) or V₂O₅ annealed at high temperatures for long hours in extremely low-oxygen environment,^[37, 38] which improves VO₂ solar transmission contrast for smart windows^[39] and its electrical resistivity contrast.^[40]

To facilitate the reduction of surface over-oxides, hydrogen gas can be carefully introduced either directly or in the forming gas (5%H₂ / 95%N₂) to reactively remove redundant oxygen atoms in the film at high temperatures.^[41] The use of forming gas can result in denser crystallization at higher temperatures and at longer hours.^[42] Note that similar reduction via solution-based chemical reaction using hydrogen-based agents has been employed to study monoclinic VO₂ (M) from V₂O₅ nanopowders and nanoparticles, known as hydrothermal process.^[27] However, as hydrothermal synthesis requires optimization of multiple chemical reaction processes during which VO₂ phase undergoes transformation into metastable phase such as VO₂ (B) and VO₂ (A), it is challenging to obtain pure monoclinic phase VO₂ (M)^[43, 44]

In this work, we demonstrate maximal infrared transmission contrast from pristine VO₂ thin film prepared by cost-effective thermal growth method involving sputtering, furnace oxidation in O₂-rich atmosphere, and surface reduction with forming gas via rapid thermal processing. Vanadium thin films of different thicknesses are sputtered onto undoped silicon wafers. Oxidation time study at 350°C is carried out to determine the fully oxidation condition with minimal surface over-oxides. Reduction time study at 500°C is performed to reach the optimal reduction where pristine VO₂ is obtained. Temperature-dependent infrared transmittance and electrical resistivity are characterized to show the evolutional IMT behaviors of the oxidized vanadium thin film with different oxide states over reduction time, which are directly revealed by X-ray diffraction measurements. Finally, complex refractive indices of pristine VO₂ thin film from this thermal growth method are fitted for both insulating and metallic phases with the help of global optimization.

2. Results and Discussion

Fabrication process to obtain high quality thermally grown VO₂ thin films consists of vanadium deposition via sputtering, thermal oxidation in O₂-rich furnace, and surface reduction via rapid thermal annealing with forming gas, as depicted in Fig. 1 (See Sec. 4 for experimental details). To begin with, vanadium films of different thicknesses are deposited with DC sputtering (Fig. 1a) onto double-side polished undoped silicon wafers. Three different thicknesses of vanadium are deposited separately (100 nm, 150 nm, and 200 nm) which are studied for optimal oxidation time to determine largest possible infrared transmittance contrast. Next, the sputtered vanadium thin films are thermally oxidized at 350°C in a muffle furnace rich of O₂ (Fig. 1b). Insufficient oxidation will leave some vanadium unoxidized, which leads to lower transmission in the insulating phase. Excessive oxidation will lead to high-oxides such as V₂O₅ on the film surface, which would yield higher transmission in the metallic phase. In this study, optimal oxidation time is determined when the infrared transmittance at insulating phase saturates. Note that under this fully oxidation condition, all the vanadium should be just oxidized, while there still exists some amount of surface over-oxides due to large O₂ concentration in the furnace atmosphere. Lastly, the fully oxidized vanadium thin films are taken for surface reduction at 500°C in rapid thermal processing with 0.1 LPM forming gas (5%H₂ / 95%N₂) as a reduction agent (Fig. 1c). The reduction time is further studied to achieve the best quality of VO₂ thin films with all surface over-oxides reduced to VO₂ without over-reducing it to lower-oxides or vanadium, under which the infrared transmission contrast is maximized upon VO₂ phase transition. Temperature-dependent infrared spectrometry, temperature-dependent electrical resistivity measurements, and X-Ray diffraction characterizations (See Sec. 4 for experimental details) are carried out to fully understand the effects of oxidation time and reduction time on the oxidation states, IMT phase transition behaviors, and film compositions. In addition, the film thickness is also measured with profilometry for 150-nm-thick vanadium thin film after sputtering (150±2.6 nm), fully oxidation (315±14 nm), and optimal reduction (304±16 nm) (See Fig. S1) for fitting the complex refractive indices of thermally grown pristine VO₂ thin film.

Figure 2(a) summarizes how oxidation time in the O₂-rich muffle furnace at 350°C for vanadium thin films of three different thicknesses affects the infrared transmission contrast between the insulating phase (measured at 25°C) and metallic phase (measured at 95°C). The optimal oxidation time is determined once the 54% transmittance at $\lambda = 8 \mu\text{m}$ line (dashed line)

is reached with all the vanadium just fully oxidized, at which transmittance saturates over time. Further oxidation will lead to more over-oxidation from VO_2 to V_2O_5 at the film surface, which barely changes the infrared transmission at 25°C as both insulating VO_2 and V_2O_5 are infrared transparent but significantly increases the infrared transmission at 95°C as more VO_2 in lossy metallic phase is over-oxidized into transparent V_2O_5 . Accordingly, 100 nm, 150 nm and 200 nm vanadium were found to have optimal oxidation time to be 400 mins, 950 mins, and 1700 mins. Note that, at the optimal oxidation time, the transmission contrast is not necessarily the largest due to the fact that surface over-oxides could exist in O_2 -rich furnace atmosphere before all the vanadium within the film is oxidized. More importantly, during the oxidation process it should be ensured that all the vanadium is fully oxidized, and the transmission contrast can be maximized by surface reduction process later. As optimal oxidation time is passed, notable increase in transmittance can be observed for both insulating and metallic phase (Fig. 2b). Due to growth of transparent V_2O_5 with low index of $n \sim 2.2$ (at $\lambda = 2 \mu\text{m}$)^[45] on the surface, slight anti-reflection effect results in transmittance increment in shorter wavelengths ($\lambda < 8 \mu\text{m}$). Likewise, transmittance dips around $10 \mu\text{m}$ and $12 \mu\text{m}$ wavelengths associated with O-V-O bond and V=O bond respectively^[46] enlarge over time. Note that, at the metallic phase of fully oxidized VO_2 thin films, there are 26%, 11%, 9% difference (at $9 \mu\text{m}$) for 100 nm, 150 nm, and 200 nm vanadium respectively compared to that of the expected spectra. This corresponds to 24% of the expected maximized transmittance contrast ($\Delta\tau = 46\%$ for 150 nm) between insulating and metallic phase. Hence, the adverse effect of surface over-oxides cannot be neglected.

In order to achieve the best quality of thermally grown VO_2 thin films and thus maximize the infrared transmission contrast upon phase transition, reduction of surface over-oxides to VO_2 is carried out via rapid thermal processing at 500°C with forming gas (5% H_2 / 95% N_2). Reduction process with different durations at 500°C is conducted for the fully oxidized 150-nm vanadium thin film. As shown in Fig. 3(a), the infrared transmittance is measured at insulating (25°C) and metallic (95°C) phases for each reduction duration of 0 mins, 45 mins, 60 mins, 70 mins, 77.5 mins, and 80 mins. Note that 0.1 LPM forming gas is purged at atmospheric pressure throughout heating, reduction and cooling stages. Therefore, even with 0 mins reduction duration at 500°C , slight reduction could occur during heating and cooling stages at a rate of 10°C per second. This effect can be observed from 0 min reduction duration in the FTIR transmission, which decreases in the insulating phase and slightly increases in the metallic phase compared to those right after fully oxidation. The infrared transmission in the insulating

phase of VO₂ measured at 25°C further decreases with 45 mins of reduction at 500°C, but it starts bouncing back with 60 and 70 mins of reduction, and finally reaches the expected spectrum for optimally reduced VO₂ film after 77.5 mins. On the other hand, the transmission in the metallic phase measured at 95°C continues to decrease slowly with longer reduction time and matches with that of optimally reduced VO₂ thin film after 77.5 mins of reduction. However, when the reduction time further increases by another 2.5 mins, the infrared transmittance at the insulating phase plummets from around 0.5 to 0.15. Correspondingly, Figure 3(b) shows that the transmittance contrast $\Delta \tau$ at 9 μm wavelength between the insulating and metallic phases is about 0.29 with 0 min reduction, decreases to 0.21 after 45 mins of reduction, gradually increases to a maximum of 0.46 with optimal reduction 77.5 mins, and suddenly drops to 0.14 with 80 mins of reduction.

The evolutional behavior of the thermally oxidized vanadium thin film on reduction time can be understood by the phase diagram of different vanadium oxide states,^[43] based on which it is hypothesized that high-oxides such as V₂O₅ at the film surface reduces to V₆O₁₃ first and then VO₂ with optimal time, and finally V₂O₃ with excessive time, as depicted in Fig. 3(b). To confirm it, Grazing Incident X-ray Diffraction scans are performed to reveal the vanadium oxide states at the film surface and within the film after different reduction durations (Fig. 4). Starting with fully oxidized (no reduction) sample (blue solid lines), as-expected high-oxides V₂O₅ peak ($2\theta = 20.4^\circ$) is detected at both the surface and within the film. Presence of V₃O₇ ($2\theta = 55.0^\circ$) is also observed, which overlaps with VO₂ (M) (220) within 0.5° . Since the existence of VO₂ is confirmed with FTIR measurement on insulating and metallic phase with small transmittance contrast, it is considered that the oxidation in oxygen-rich environment results high-oxides V₂O₅ and V₃O₇ at the surface of VO₂ film. With 500°C reduction from 0 min to 45 mins, disappearing V₂O₅ and V₃O₇ peaks and emerging V₆O₁₃ peak (50.4°) are observed in the XRD spectra on the film surface. In addition, VO₂ (B) phase (55.5°) shows up in the XRD spectra within the film along with multiple small VO₂ (M) phase peaks. Note that B-phase is a metastable VO₂ phase which was observed in hydrothermal reduction process as V₂O₅ \rightarrow VO₂(B) \rightarrow VO₂(M).^[27, 47] As the phase transition temperature for both V₆O₁₃ and VO₂ (B) are less than 300 K,^[48, 49] both behave metallic above the room temperature, which leads to decreasing transmission contrast observed in the FTIR spectra. With 45 mins of reduction, the transmittance contrast reaches its minimum as all the V₂O₅ vanishes with highest volumetric ratio of V₆O₁₃ and VO₂(B).

With longer reduction time, both V_6O_{13} and $VO_2(B)$ are further reduced to $VO_2(M)$ with the transmission contrast increases as seen from the FTIR spectra with 60 and 70 mins of reduction (Fig. 3(a)). After an optimal reduction time of 77.5 mins, only $VO_2(M)$ phase is observed on the film surface and within the film at 37.1° , 42.4° and 55.6° corresponding to (200), (210), and (220) orientations without any other oxide state or phase, which is consistent with VO_2 fabricated via MBE, PLD and hydrothermal process.^[50-52] This clearly suggests an optimal reduction of thermally grown VO_2 thin film with surface over-oxides to the pristine polycrystalline monoclinic VO_2 whose insulator-to-metal phase transition is expected to occur around $68^\circ C$.^[43] As a result, transmittance contrast is maximized after 77.5 mins of optimal reduction. With further reduction, VO_2 starts to reduce to lower oxide V_2O_3 whose peak is observed in the XRD spectra after 80 mins of reduction. Note that V_2O_3 is metallic at room temperature with phase transition temperature around 160 K,^[48] which leads to diminishing contrast in transmittance measured at $25^\circ C$ and $95^\circ C$. Excessive reduction at even longer time could finally reduce the oxidized film back to vanadium completely.

In order to fully understand the evolutional IMT behaviors such as phase transition temperature and thermal hysteresis of the oxidized vanadium films reduced after different duration, comprehensive temperature-dependent optical characterizations are carried out. Figure 5 presents the infrared transmittance spectra measured between $25^\circ C$ and $95^\circ C$ in $5^\circ C$ intervals ($2^\circ C$ interval within phase transition region) upon heating and cooling for the fully oxidized 150-nm vanadium thin film after (a) no reduction, (b) slight reduction with 0 min, (c) optimal reduction with 77.5 mins, and (d) over reduction with 80 mins via rapid thermal processing. Figure 6 shows the corresponding heating-cooling curves as a function of temperature for transmittance at $9 \mu m$ wavelength, as well as the derivative with respect to temperature for each case. Without reduction gradual change in transmittance spectra is observed (Fig. 5a) and phase transition takes place during heating around $66^\circ C$ (where largest derivative magnitude exists) or $49^\circ C$ upon cooling (Fig. 6a). The existence of over-oxides on the surface leads to not only a smaller transmittance contrast of 23% (at $\lambda = 9 \mu m$) but also a wider thermal hysteresis of $17^\circ C$. Slight reduction occurs with forming gas purging during heating up and cooling down stages of rapid thermal annealing even with 0 min at $500^\circ C$, which improves the transmission contrast by 6% with similar thermal hysteresis width of $18.5^\circ C$ (Fig. 5b and 6b).

With optimal reduction time of 77.5 mins, pristine VO₂ (M) is obtained throughout the entire film, which leads to not only the maximal transmission of 46% at $\lambda = 9 \mu\text{m}$ but also a sharp IMT phase transition of about 15°C and a narrow thermal hysteresis of only 4°C (Fig. 6c). In particular, the derivative curve exhibits a full width at a half maximum (FWHM) of 2.2°C around 66°C upon heating and a FWHM of 2.8°C around 62°C upon cooling. The average phase transition temperature is taken as 64°C, which is slightly lower than typically reported 68°C.^[43] Similar behavior has also been observed in MBE-based VO₂ with narrow thermal hysteresis.^[16] Factors such as grain size and crystallinity could also affect hysteresis width and transition temperature slightly.^[53, 54] Compared to that without any reduction, the optimal reduction process has narrowed hysteresis width by 13°C, and augmented the transmission contrast $\Delta\tau_\lambda$ at $\lambda = 9 \mu\text{m}$ by another 23% with one-fold enhancement. For the over reduced VO₂ thin film after 80 mins rapid thermal annealing, due to the formation of V₂O₃ the infrared transmission drops (Fig. 5d) and thermal hysteresis widens to 23.5°C (Fig. 6d). The evolutionary study on the reduction time clearly indicates optimal reduction is required to get rid of surface over-oxides (i.e., V₂O₅, V₆O₁₃) and avoid the formation of low-oxide (V₂O₃) for obtaining pristine monolithic VO₂ from thermal growth method with maximal transmission contrast, sharp IMT phase transition and narrow thermal hysteresis.

To confirm the evolutionary IMT behaviors from fully oxidized 150-nm vanadium films reduced after different durations, temperature-dependent electrical resistivity is measured (See Sec. 4 for experimental details) between 25°C and 95°C in 5°C intervals (2°C interval within phase transition region) upon heating and cooling. Without reduction (Fig. 7a), the resistivity exhibits about 50 times of variation upon a broad IMT phase transition and a wide thermal hysteresis loop due to the existence of surface over-oxides. With 0-min rapid thermal processing (Fig. 7b), slight reduction occurs with insulating surface over-oxides start to be reduced to metallic V₆O₁₃ or VO₂, which leads to 10² times of variation in resistivity upon similar broad phase transition. With the thermally grown VO₂ thin film after 77.5-min rapid thermal processing, the resistivity achieves a variation of 10³ times upon phase transition, which is comparable to that those pristine VO₂ fabricated by MBE or PLD techniques,^[16, 55, 56] thanks to the removal of surface over-oxides from the optimal reduction. In addition, sharp phase transition and narrow thermal hysteresis are clearly seen from the resistivity derivative curves, which is consistent with the observation from the optical characterizations. Lastly, over reduction after 80-min RTP diminishes the variation of resistivity down to only 25 times upon broad phase transition due to

existence of V_2O_3 with transition temperature at 160 K,^[48] which significantly decreases the electrical resistivity from $2000 \Omega \cdot \text{cm}$ (pristine VO_2) to $30 \Omega \cdot \text{cm}$ at room temperature as a result of its metallic behavior.

Finally, refractive index n and extinction coefficient κ of optimally reduced 300-nm-thick polycrystalline VO_2 (M) thin film are extracted for both the insulating and metallic phases by fitting the measured transmittance and reflectance spectra. With the help of global optimization (See Sec. 4 for details), excellent agreement is obtained between the fitted and measured spectra, as shown in Fig. 8(a) and (b) for the insulating and metallic phase, respectively. The relative root-mean square errors (RMSE) are 1.55% (transmittance) and 2.59% (reflectance) for the insulating phase, and 11% (transmittance) and 3.82% (reflectance) for the metallic phase via the Drude model. Transmittance at metallic phase has relatively larger RMSE value due to its small values $< 4\%$. As shown in Fig. 8(c), fitted refractive index n and extinction coefficient κ of the optimal thermally grown VO_2 for the insulating phase agree well with the literature data for single-crystalline VO_2 (ordinary component)^[57] except for weaker phonon absorption in the long wavelengths, which is understandable considering its polycrystalline nature. On the other hand, the fitted (n, k) values of the optimal thermally grown VO_2 in the metallic phase match well with the those for single-crystalline VO_2 ^[57] as seen in Fig. 8(d), with fitted Drude parameters of high frequency constant $\epsilon_\infty = 3.39$, plasma frequency $\omega_p = 3.16 \times 10^{15}$ rad/s, and scattering rate $\gamma = 9.17 \times 10^{14}$ rad/s. This confirms the success in removing the surface oxides and avoiding the formation of low-oxide with optimal reduction process via rapid thermal processing to obtain pristine VO_2 thin film from thermal growth method with maximal infrared transmission. See Figure S2 for comparison on infrared (n, k) values of high-quality VO_2 prepared by other fabrication methods such as reactive sputtering, ALD and PLD.^[18, 21, 56]

3. Conclusion

In summary, this work has demonstrated the successful fabrication of pristine VO_2 thin film via furnace oxidation in oxygen-rich atmosphere and rapid thermal reduction of surface oxides with forming gas (5% H_2 / 95% N_2). The contrast in infrared transmission upon VO_2 phase transition is maximized with 2-fold enhancement compared to the oxidized vanadium film without reduction. The study on the reduction time reveals the evolutionary behavior in infrared transmission variation upon phase transition which is due to hydrothermal process among

different vanadium oxide states directly measured by the XRD. Temperature dependent electrical resistivity of the oxidized vanadium films reduced over different durations also shows consistent phase transition behaviors with 3 orders of magnitude drop. Sharp phase transition and narrow thermal hysteresis within $2 \sim 4^\circ\text{C}$ are achieved from optimally reduced VO_2 thin film in both infrared transmittance and electrical resistivity, comparable to best quality of VO_2 prepared by other sophisticated fabrication techniques.^[16, 26, 37, 50, 58] This thermal growth method could lead to scalable fabrication of pristine VO_2 thin films and tunable coatings for applications in adaptive thermal control,^[3, 4, 23, 59-61] thermal rectification,^[13, 14, 62, 63] high-resolution thermal sensing,^[64] and thermal camouflage.^[65-68]

4. Experimental Section

Vanadium deposition: Undoped double-side polished silicon wafers (280 μm thick, 2 inch in diameter, $\rho > 10,000 \Omega\cdot\text{cm}$, (100), UniversityWafer, Inc.) are used as substrates, which are cleaned with acetone and isopropyl alcohol and dried with nitrogen gas before sample fabrication. First, vanadium (purity $> 99.9\%$ sputtering target, Kurt J. Lesker) is deposited onto the undoped silicon wafers via sputtering (Lesker PVD75 sputterer) at a rate of 0.9 \AA/s with DC power of 125 W in vacuum pressure of 5×10^{-6} Torr and process pressure of 4 mTorr with Ar gas flow. Note that a time period of 10 mins is given to reach stable deposition rate before opening the shutter for 27 mins to deposit about 150 nm vanadium thin film onto the substrate. Adequate time about 30 mins is also given for the samples to sufficiently cool down to prevent any oxidation after venting the vacuum chamber to ambient. A glass slide is utilized to cover a very small part of the silicon wafer, which creates a step after deposition for thin film thickness measurement with the profilometer (Bruker DektakXT, Fig. S3) later.

Oxidation and reduction: The sputtered vanadium is oxidized at 350°C in air (20.9% oxygen) for a certain amount of time in a muffle furnace (KSL-1100X, MTI Corporation). The oxidation process starts with heating at 10°C per min from room temperature to 350°C with 5 LPM nitrogen gas flow (purity 99.99%). Then dry air (O_2 : 20-22%) is supplied at 2.5 LPM into the furnace for 10 minutes. The temperature is maintained at 350°C within $\pm 1^\circ\text{C}$ by PID control for a given amount of oxidation time, after which the sample is cooled down with heater turned off and 5 LPM nitrogen purging until it reaches the room temperature. Note that high-purity nitrogen purging is to minimize oxidation during heating and cooling stages. After furnace

oxidation, surface reduction is conducted in the rapid thermal annealing system (AS-ONE 100 RTP, ANNEALSYS) at 500°C with the forming gas (5% H_2 /95% N_2) flowing above the sample that sits on 4-inch graphite susceptor. The process starts with vacuum pumping for 10 seconds to clear out any gas residues followed by purging with forming gas at 1 LPM. Once the chamber is purged back to atmospheric pressure, the sample is heated at 10°C per second ramping rate with 0.1 LPM forming gas. After the temperature reaches 500°C, the forming gas flowrate is fixed for a given duration of reduction time. The cooling process takes place at the same forming gas flowrate with heating off until the temperature drops to 100°C.

Material characterization: Temperature-dependent infrared transmittance and reflectance of VO_2 samples are measured with an FTIR spectrometer (Nicolet iS50, Thermo Fisher Scientific) at (near) normal direction from 2 μm to 20 μm in wavelength with 4 cm^{-1} resolution and each spectrum averaged over 32 scans. Aluminum mirror is used as the reference for reflection measurement in an accessory (PIKE10, PIKE Technologies). See Fig. S4 for FTIR setup. Temperature-dependent electrical resistivity is measured with a home-made four-probe station (Fig. S5) along with a source meter (Keithley 2401). The resistivity is calculated from the slope of I-V curve (S) and thickness (t) as $\rho = C\pi St/\ln 2$, where C is the geometrical factor. Sample temperature is varied with a custom built temperature stage made of a thermoelectric heater and a PID temperature controller along with K-type thermocouples. Steady state condition is achieved after the sample temperature reaches setpoint for 5 mins with fluctuation less than $\pm 1^\circ\text{C}$. Lastly, grazing incidence X-ray diffraction (GIXRD, Rigaku SmartLab) are performed with Cu $K\alpha$ source. The 2θ scans are conducted with angle of incidence $\omega = 0.5^\circ$ and 2.0° to probe the surface and within the thin film, respectively. The obtained diffraction patterns were compared with database (HighScore Plus) as well as literature that navigate the rapid thermal processing by forming gas.

Extraction of complex refractive index: The wavelength-dependent dielectric function for the insulating phase of VO_2 is fitted using Bayesian optimization (MATLAB, bayesopt) for refractive index n ($4 \geq n \geq 1$) and extinction coefficient κ ($10 \geq \kappa \geq 0$). The optimization takes place using the acquisition function, which integrates the positive improvement of Gaussian distribution function, acquiring next probable candidate that can update the current objective function^[69] as

$$f_{\lambda} = \max(|\tau_{\lambda,\text{measured}} - \tau_{\lambda,\text{theory}}|, |\rho_{\lambda,\text{measured}} - \rho_{\lambda,\text{theory}}|) \quad (3)$$

where τ is the transmittance, ρ is the reflectance and λ is the wavelength. Theoretical transmittance and reflectance are calculated with transfer matrix method (TMM) incorporated with ray tracing^[70] for 300-nm VO₂ thin film on 280- μ m undoped silicon wafer. On the other hand, Drude model is fitted for vanadium and metallic phase of VO₂ thin films with global search (MATLAB *gs*) along with gradient-based minimization method (MATLAB *fmincon*). The optimization is conducted by providing the initial guess which is used to find parameters that minimize the objective function. With obtained population of candidates from gradient-based methods, global search utilizes scatter search algorithms to generate potential points that hunts for optimal solutions and minimal objective functions.^[71] Thus, it helps to reduce locating local minimum found by gradient-based method, which requires superlative initial guess. The objective function for fitting Drude model is written as,

$$f = \sqrt{\frac{1}{N} \sum_{j=1}^N \left(\frac{\alpha_{\text{measured}} - \alpha_{\text{theory}}}{\alpha_{\text{measured}}} \right)^2} \quad (4)$$

where $\alpha = 1 - \tau - \rho$ is the absorptance spectrum and N represents number of wavelengths. Optimization is divided into two sections. First, all three parameters of the Drude model (high frequency constant ε_{∞} , plasma frequency ω_p , scattering rate γ) and thickness d are fitted together. Here, Drude model is expressed as,^[70]

$$\varepsilon = \varepsilon_{\infty} - \frac{\omega_p^2}{\omega(\omega + i\gamma)} \quad (5)$$

Second, using the fitted plasma frequency and scattering rate, high frequency constant and thickness is adjusted by replacing absorptance α by transmittance τ in Eq. (4). Hence, the Drude model for both vanadium (See Fig. S6) and metallic phase of VO₂ (Fig. 8) is determined from transmittance and reflectance spectra measured from FTIR. The fitting is validated with 300 nm-thick SiO₂ using Eq. (3) to mimic VO₂ insulating phase and 10 nm Ag to mimic VO₂ metallic phase using Eq. (4) as shown in Fig. S7.

Acknowledgements

This work was supported by the National Science Foundation (NSF) under Grant No. CBET-2212342. We would like to thank ASU NanoFab and Goldwater Center for use of their nanofabrication and characterization facilities.

Conflict of Interests

The authors do not declare conflict of interest.

Author Contributions

K.A. fabricated the samples, characterized optical and electrical properties, fitted the complex refractive indices, prepared the figures, and drafted the manuscript. V.K.R. performed XRD scans. L.W. conceived the idea, supervised the work, secured the funding, and revised the manuscript. All authors have reviewed and approved the final version of the manuscript.

References

- [1] M. Li, Y. Cheng, C. Fang, X. Zhang, H. Han, Y. Zhang, *Sol. Energy Mater. Sol. Cells* **2024** 275, 113040.
- [2] S. Taylor, Y. Yang, L. Wang, *J. Quant. Spectrosc. Radiat. Transf.* **2017** 197, 76-83.
- [3] S. Taylor, L. Long, R. McBurney, P. Sabbaghi, J. Chao, L. Wang, *Sol. Energy Mater. Sol. Cells* **2020** 217, 110739.
- [4] R. Yu, B.K. Shrewsbury, C. Wu, H. Kumarasubramanian, M. Surendran, J. Ravichandran, M.L. Povinelli, *Appl. Phys. Lett.* **2024** 125, 121117.
- [5] S. Bhupathi, S. Wang, G. Wang, Y. Long, *Nanophotonics* **2024** 13, 711-723.
- [6] B. Ko, T. Badloe, J. Rho, *Chem. Nano. Mat.* **2021** 7, 713-727.
- [7] X. Ao, B. Li, B. Zhao, M. Hu, H. Ren, H. Yang, J. Liu, J. Cao, J. Feng, Y. Yang, Z. Qi, L. Li, C. Zou, G. Pei, *PNAS* **2022** 119, e2120557119.
- [8] M. Liu, X. Li, L. Li, L. Li, S. Zhao, K. Lu, K. Chen, J. Zhu, T. Zhou, C. Hu, Z. Lin, C. Xu, B. Zhao, G. Zhang, G. Pei, C. Zou, *ACS Nano* **2023** 17, 9501-9509.
- [9] C. Wan, D. Woolf, C.M. Hessel, J. Salman, Y. Xiao, C. Yao, A. Wright, J.M. Hensley, M.A. Kats, *Nano Lett.* **2022** 22, 6-13.
- [10] J. Chao, S. Taylor, L. Wang, *Int. J. Heat Mass Transf.* **2022** 186, 122515.
- [11] J. Rensberg, Y. Zhou, S. Richter, C. Wan, S. Zhang, P. Schöppe, R. Schmidt-Grund, S. Ramanathan, F. Capasso, M.A. Kats, *Phys. Rev. Appl.* **2017** 8, 014009.
- [12] M.A. Kats, D. Sharma, J. Lin, P. Genevet, R. Blanchard, Z. Yang, M.M. Qazilbash, D.N. Basov, S. Ramanathan, F. Capasso, *Appl. Phys. Lett.* **2012** 101, 221101.
- [13] K. Ito, K. Nishikawa, H. Iizuka, H. Toshiyoshi, *Appl. Phys. Lett.* **2014** 105, 253503.
- [14] A. Fiorino, D. Thompson, L. Zhu, R. Mittapally, S.A. Biehs, O. Bezencenet, N. El-Bondry, S. Bansropun, P. Ben-Abdallah, E. Meyhofer, P. Reddy, *ACS Nano* **2018** 12, 5774-5779.
- [15] L.L. Fan, S. Chen, Y.F. Wu, F.H. Chen, W.S. Chu, X. Chen, C.W. Zou, Z.Y. Wu, *Appl. Phys. Lett.* **2013** 103, 131914.

- [16] J. Bian, M. Wang, H. Sun, H. Liu, X. Li, Y. Luo, Y. Zhang, *J. Mater. Sci.* **2016** *51*, 6149-6155.
- [17] M. Benkahoul, M. Chaker, J. Margot, E. Haddad, R. Kruzelecky, B. Wong, W. Jamroz, P. Poinas, *Sol. Energy Mater. Sol. Cells* **2011** *95*, 3504-3508.
- [18] C. Wan, Z. Zhang, D. Woolf, C.M. Hessel, J. Rensberg, J.M. Hensley, Y. Xiao, A. Shahsafi, J. Salman, S. Richter, Y. Sun, M.M. Qazilbash, R. Schmidt - Grund, C. Ronning, S. Ramanathan, M.A. Kats, *Ann. Phys. (N.Y.)* **2019** *531*, 1900188.
- [19] H. Ma, X. Xiao, Y. Wang, Y. Sun, B. Wang, X. Gao, E. Wang, K. Jiang, K. Liu, X. Zhang, *Sci. Adv.* **2021** *7*, eabk3438.
- [20] C. Cao, B. Hu, G. Tu, X. Ji, Z. Li, F. Xu, T. Chang, P. Jin, X. Cao, *ACS Appl Mater Interfaces* **2022** *14*, 28105-28113.
- [21] A.M. Morsy, M.T. Barako, V. Jankovic, V.D. Wheeler, M.W. Knight, G.T. Papadakis, L.A. Sweatlock, P.W.C. Hon, M.L. Povinelli, *Sci. Rep.* **2020** *10*, 13964.
- [22] M. Currie, M.A. Mastro, V.D. Wheeler, *Opt. Mater. Express* **2017** *7*, 1697-1707.
- [23] K. Sun, W. Xiao, C. Wheeler, M. Simeoni, A. Urbani, M. Gaspari, S. Mengali, C. de Groot, O.L. Muskens, *Nanophotonics* **2022** *11*, 4101-4114.
- [24] D. Fu, K. Liu, T. Tao, K. Lo, C. Cheng, B. Liu, R. Zhang, H.A. Bechtel, J. Wu, *J. Appl. Phys.* **2013** *113*, 043707.
- [25] R. McGee, A. Goswami, B. Khorshidi, K. McGuire, K. Schofield, T. Thundat, *Acta Materialia* **2017** *137*, 12-21.
- [26] N. Wang, S. Magdassi, D. Mandler, Y. Long, *Thin Solid Films* **2013** *534*, 594-598.
- [27] M. Li, S. Magdassi, Y. Gao, Y. Long, *Small* **2017** *13*, 1701147.
- [28] D. Guo, C. Ling, C. Wang, D. Wang, J. Li, Z. Zhao, Z. Wang, Y. Zhao, J. Zhang, H. Jin, *ACS Appl Mater Interfaces* **2018** *10*, 28627-28634.
- [29] S. Taylor, L. Long, L. Wang, *Thin Solid Films* **2019** *682*, 29-36.
- [30] P. Guo, Z. Biegler, T. Back, A. Sarangan, *Thin Solid Films* **2020** *707*, 138117.
- [31] P. Clauws, J. Vennik, *Phys. Status Solidi* **1976** *76*, 707-713.
- [32] Y.-K. Dou, J.-B. Li, M.-S. Cao, D.-Z. Su, F. Rehman, J.-S. Zhang, H.-B. Jin, *Appl. Surf. Sci.* **2015** *345*, 232-237.
- [33] A.J. Santos, B. Lacroix, M. Dominguez, R. Garcia, N. Martin, F.M. Morales, *Surf. Interfaces* **2021** *27*, 101581.
- [34] A.C. García-Wong, D. Pilloud, S. Bruyère, D. Mangin, S. Migot, J.F. Pierson, F. Capon, *J. Materiomics* **2021** *7*, 657-664.
- [35] G. Rampelberg, B. De Schutter, W. Devulder, K. Martens, I. Radu, C. Detavernier, *J. Mater. Chem. C* **2015** *3*, 11357-11365.
- [36] M.H. Lee, Y. Kalcheim, J.D. Valle, I.K. Schuller, *ACS Appl Mater Interfaces* **2021** *13*, 887-896.
- [37] J. Li, Z. An, W. Zhang, L. Hui, Z. Qin, H. Feng, *Appl. Surf. Sci.* **2020** *529*, 147108.
- [38] F. Xia, L. Yang, B. Dai, Z. Yang, L. Xu, G. Gao, C. Sun, Z. Song, V. Ralchenko, J. Zhu, *Surf. Coat. Tech.* **2021** *405*, 126637.
- [39] H.-C. Ho, Y.-C. Lai, K. Chen, T.D. Dao, C.-H. Hsueh, T. Nagao, *Appl. Surf. Sci.* **2019** *495*, 143436.
- [40] Z. Zhang, F. Zuo, C. Wan, A. Dutta, J. Kim, J. Rensberg, R. Nawrodt, H.H. Park, T.J. Larrabee, X. Guan, Y. Zhou, S.M. Prokes, C. Ronning, V.M. Shalaev, A. Boltasseva, M.A. Kats, S. Ramanathan, *Phys. Rev. Appl.* **2017** *7*, 034008.
- [41] S.A. Corr, M. Grossman, Y. Shi, K.R. Heier, G.D. Stucky, R. Seshadri, *J. Mater. Chem.* **2009** *19*, 4362-4367.
- [42] S.A. Corr, M. Grossman, J.D. Furman, B.C. Melot, A.K. Cheetham, K.R. Heier, R. Seshadri, *Chem Mater* **2008** *20*, 6396-6404.
- [43] V. Devthade, S. Lee, *J. Appl. Phys.* **2020** *128*, 231101.
- [44] Y. Zhang, W. Xiong, W. Chen, Y. Zheng, *Nanomaterials (Basel)* **2021** *11*, 338.

- [45] K. Schneider, *J. Mater. Sci.* **2020** *31*, 10478-10488.
- [46] K.M. Shafeeq, V.P. Athira, C.H.R. Kishor, P.M. Aneesh, *Appl. Phys. A* **2020** *126*, 586.
- [47] S. Kumar, P. Mishra, S. Singh, U. Chitnis, B. Thakur, S. Pal, S. Sinha - Ray, A. Goswami, *J. Am. Ceram. Soc.* **2024** *108*, 20293.
- [48] P. Hu, P. Hu, T.D. Vu, M. Li, S. Wang, Y. Ke, X. Zeng, L. Mai, Y. Long, *Chem. Rev.* **2023** *123*, 4353-4415.
- [49] A. Srivastava, H. Rotella, S. Saha, B. Pal, G. Kalon, S. Mathew, M. Motapothula, M. Dykas, P. Yang, E. Okunishi, D.D. Sarma, T. Venkatesan, *APL Mater.* **2015** *3*, 026101.
- [50] A.M. Makarevich, I.I. Sadykov, D.I. Sharovarov, V.A. Amelichev, A.A. Adamenkov, D.M. Tsybarenko, A.V. Plokhiih, M.N. Esaulkov, P.M. Solyankin, A.R. Kaul, *J. Mater. Chem. C* **2015** *3*, 9197-9205.
- [51] A. Boontan, E.K. Barimah, P. Steenson, G. Jose, *ACS Appl Mater Interfaces* **2023** *15*, 51606-51616.
- [52] Y. Hao, W. Xu, M. Li, S. Wang, H. Liu, X. Yang, J. Yang, *Nanomaterials (Basel)* **2022** *12*, 3534.
- [53] J.Y. Suh, R. Lopez, L.C. Feldman, R.F. Haglund, *J. Appl. Phys.* **2004** *96*, 1209-1213.
- [54] D. Brassard, S. Fourmaux, M. Jean-Jacques, J. Kieffer, M. El Khakani, *Appl. Phys. Lett.* **2005** *87*, 051910.
- [55] S.A. Bukhari, S. Kumar, P. Kumar, S.P. Gumfekar, H.-J. Chung, T. Thundat, A. Goswami, *Appl. Surf. Sci.* **2020** *529*, 146995.
- [56] H. Kim, K. Cheung, R.C.Y. Auyeung, D.E. Wilson, K.M. Charipar, A. Pique, N.A. Charipar, *Sci. Rep.* **2019** *9*, 11329.
- [57] A.S. Barker, H.W. Verleur, H.J. Guggenheim, *Phys. Rev. Lett.* **1966** *17*, 1286-1289.
- [58] S. Lee, T.L. Meyer, S. Park, T. Egami, H.N. Lee, *Appl. Phys. Lett.* **2014** *105*, 223515.
- [59] L. Long, S. Taylor, L. Wang, *ACS Photonics* **2020** *7*, 2219-2227.
- [60] S. Wang, T. Jiang, Y. Meng, R. Yang, G. Tan, Y. Long, *Science* **2021** *374*, 1501-1504.
- [61] K. Tang, K. Dong, J. Li, M.P. Gordon, F.G. Reichertz, H. Kim, Y. Rho, Q. Wang, C.-Y. Lin, C.P. Grigoropoulos, *Science* **2021** *374*, 1504-1509.
- [62] J. Zhu, K. Hippalgaonkar, S. Shen, K. Wang, Y. Abate, S. Lee, J. Wu, X. Yin, A. Majumdar, X. Zhang, *Nano Lett.* **2014** *14*, 4867-72.
- [63] C.L. Gomez-Heredia, J.A. Ramirez-Rincon, J. Ordonez-Miranda, O. Ares, J.J. Alvarado-Gil, C. Champeaux, F. Dumas-Bouchiat, Y. Ezzahri, K. Joulain, *Sci. Rep.* **2018** *8*, 8479.
- [64] K. Tang, K. Dong, C.J. Nicolai, Y. Li, J. Li, S. Lou, C.-W. Qiu, D.H. Raullet, J. Yao, J. Wu, *Sci. Adv.* **2020** *6*, eabd8688.
- [65] R. Hu, W. Xi, Y. Liu, K. Tang, J. Song, X. Luo, J. Wu, C.-W. Qiu, *Mater. Today* **2021** *45*, 120-141.
- [66] H. Ji, D. Liu, H. Cheng, C. Zhang, L. Yang, *Sol. Energy Mater. Sol. Cells* **2018** *175*, 96-101.
- [67] D. Liu, H. Ji, R. Peng, H. Cheng, C. Zhang, *Sol. Energy Mater. Sol. Cells* **2018** *185*, 210-217.
- [68] K. Tang, X. Wang, K. Dong, Y. Li, J. Li, B. Sun, X. Zhang, C. Dames, C. Qiu, J. Yao, J. Wu, *Adv. Mater.* **2020** *32*, 1907071.
- [69] J. Bergstra, R. Bardenet, Y. Bengio, B. Kégl, *Adv. Neural. Inf. Process. Syst.* **2011** *24*, 1-9.
- [70] Z.M. Zhang, *Nano/microscale heat transfer* Springer, Gewerbestrasse, **2020**.
- [71] F. Glover. *A template for scatter search and path relinking*. in *European conference on artificial evolution*. **1997**. Springer.

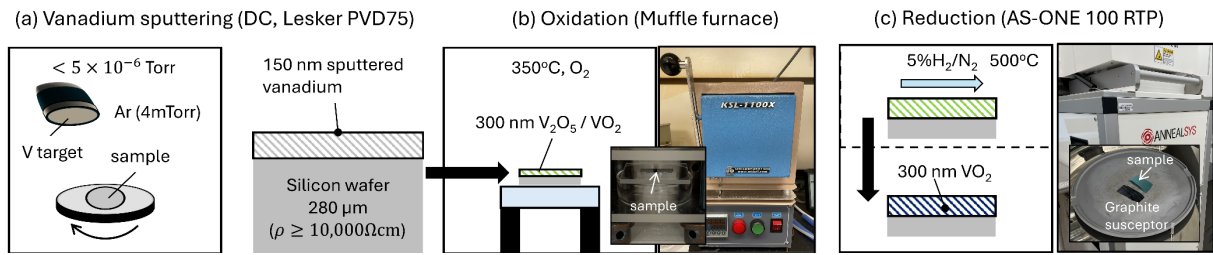


Figure 1. Fabrication process including (a) vanadium sputtering, (b) oxidation in O_2 -rich muffle furnace, and (c) surface reduction in rapid thermal annealing with forming gas (5% H_2 / 95% N_2).

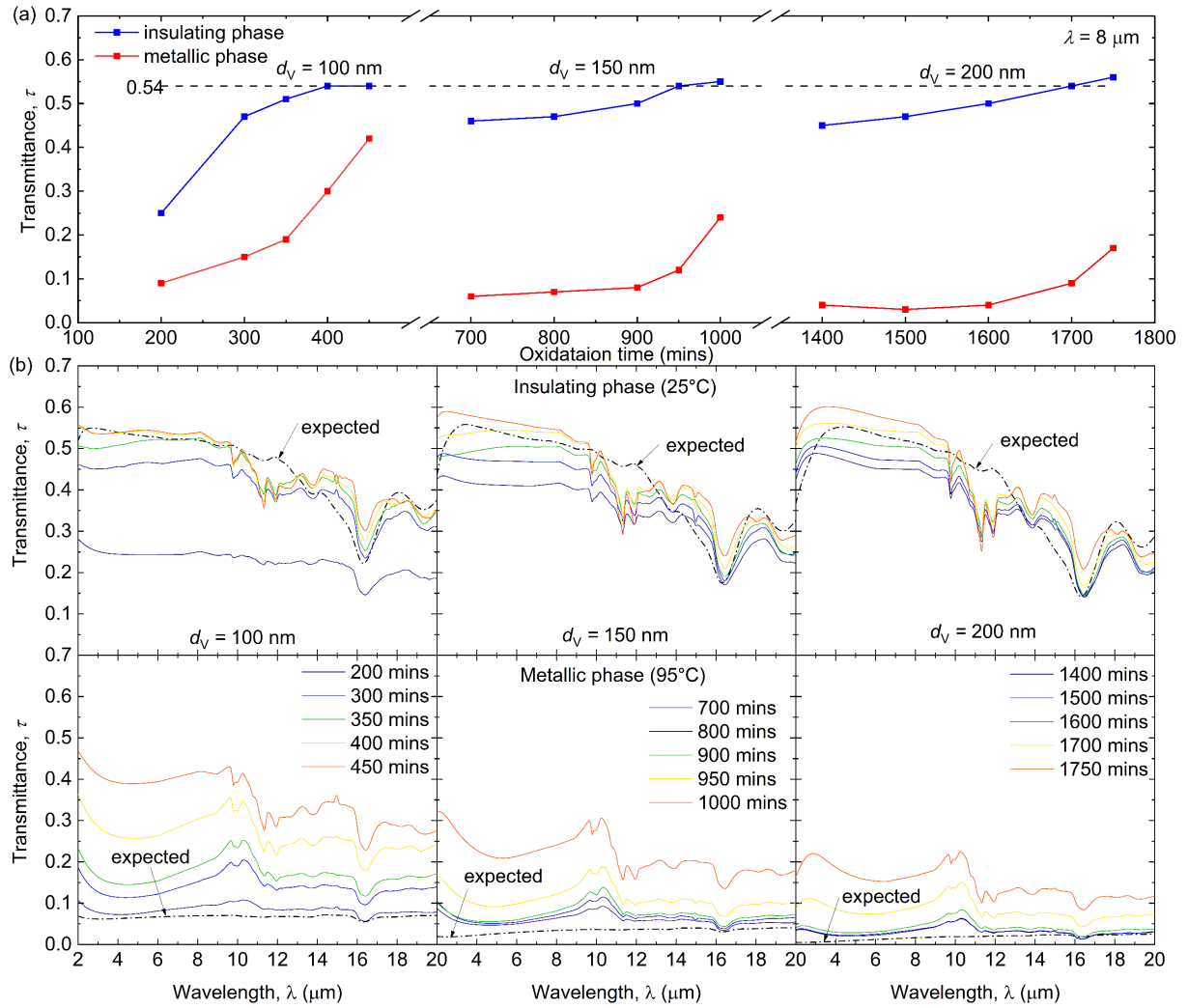


Figure 2. Thermal oxidation time study: (a) transmittance at $\lambda = 8 \mu\text{m}$ with different oxidation time for vanadium thickness $d_v = 100$ nm, 150 nm, and 200 nm; (b) transmittance spectrum at different oxidation time for both insulating (measured at 25°C) and metallic phase (measured at 95°C) for vanadium thickness $d_v = 100$ nm, 150 nm, and 200 nm.

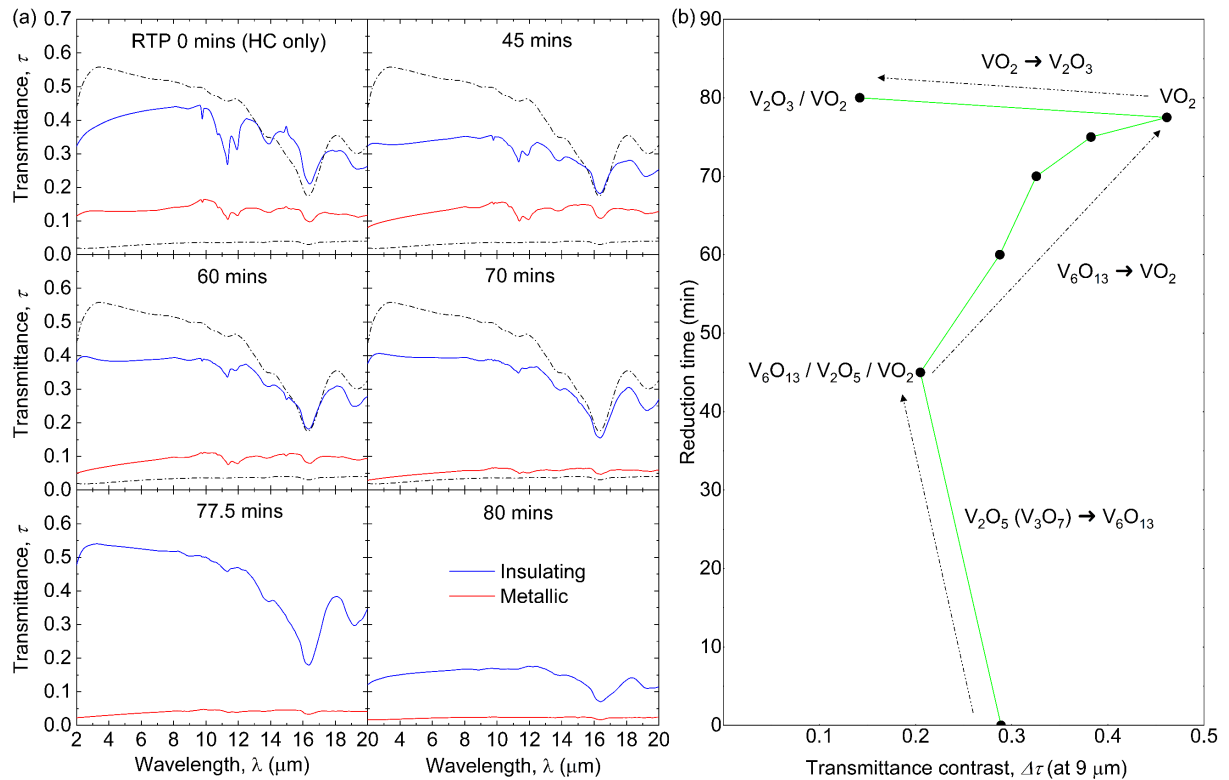


Figure 3. Surface reduction time study via rapid thermal annealing with forming gas for fully oxidized 150-nm vanadium thin film on undoped silicon wafer: (a) transmittance spectrum at insulating and metallic phase at different RTP reduction time. Dash lines show expected transmittance spectrum at insulating and metallic phase. (b) The relationship between transmittance contrast $\Delta\tau$ at $\lambda = 9 \mu\text{m}$ and reduction time.

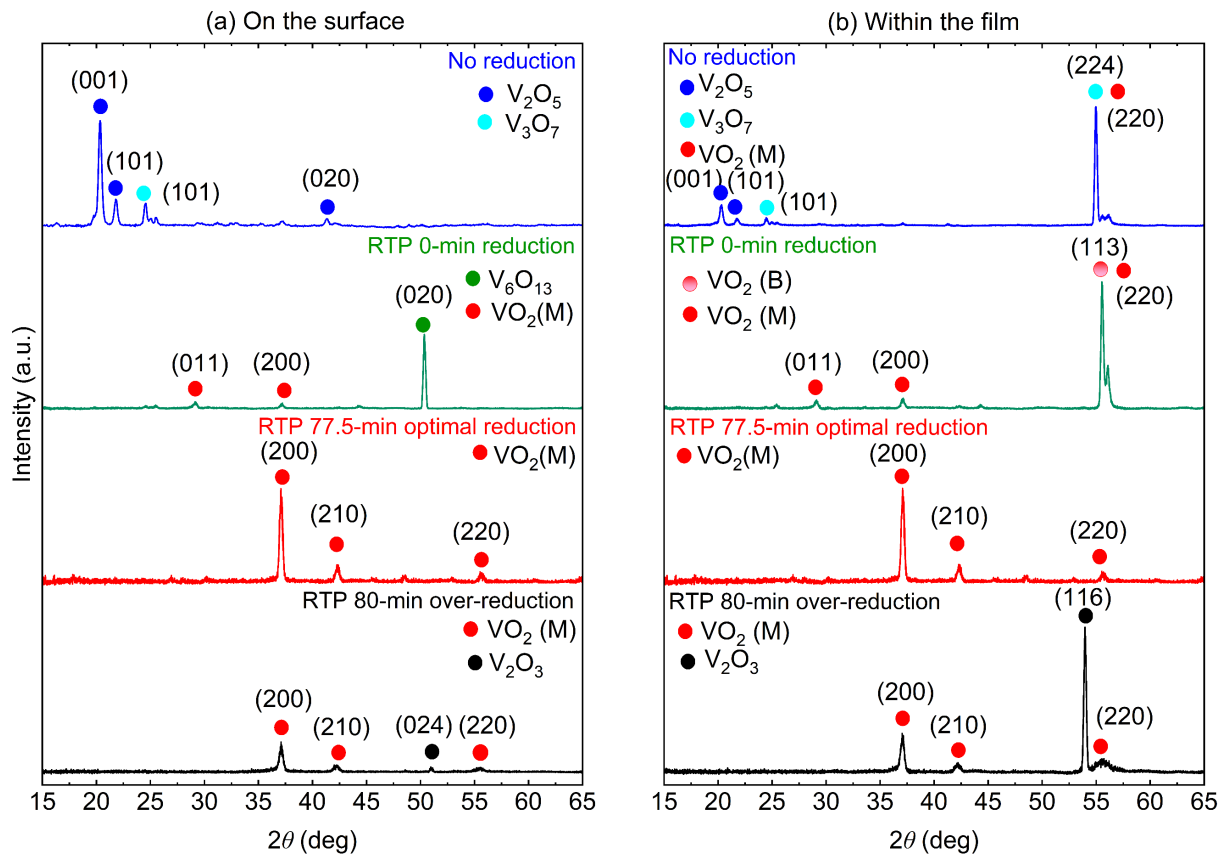


Figure 4. GIXRD diffraction patterns (a) on the surface (incident angle 0.5°) and (b) within the film (incident angle 2.0°) of fully oxidized 150-nm vanadium thin film on undoped silicon wafer after no reduction, slight reduction (RTP 0 min), optimal reduction (RTP 77.5 mins), over reduction (RTP 80 mins).

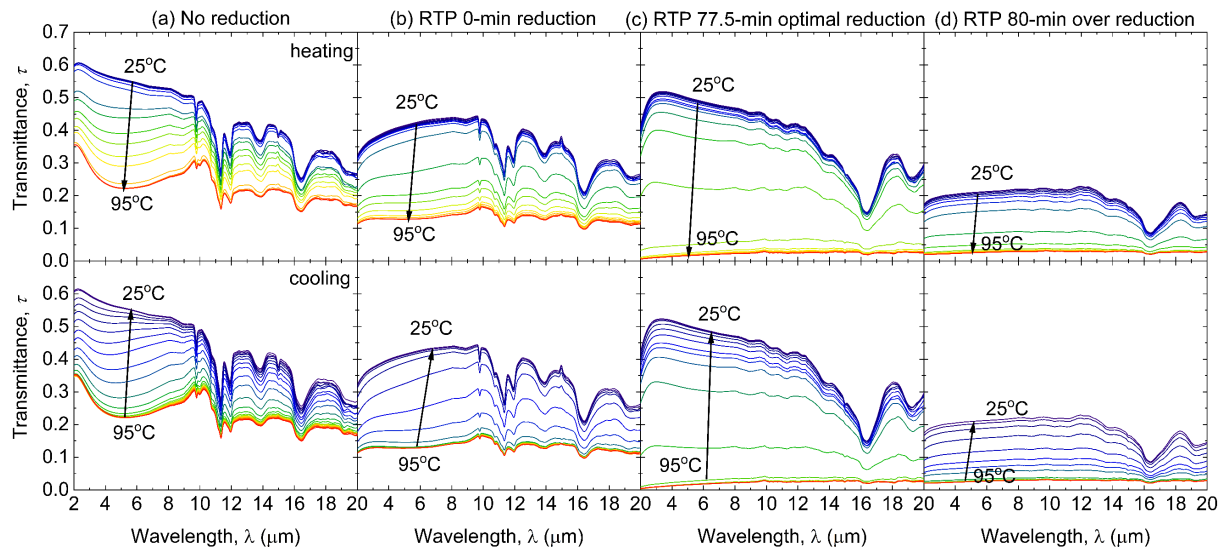


Figure 5. Insulator-to-metal phase transition behaviors of 150-nm vanadium thin film on undoped silicon wafer after (a) no reduction, (b) slight reduction (RTP 0 min), (c) optimal reduction (RTP 77.5 mins), (d) over reduction (RTP 80 mins): temperature-dependent transmittance spectrum during heating (top panel) and cooling (bottom panel).

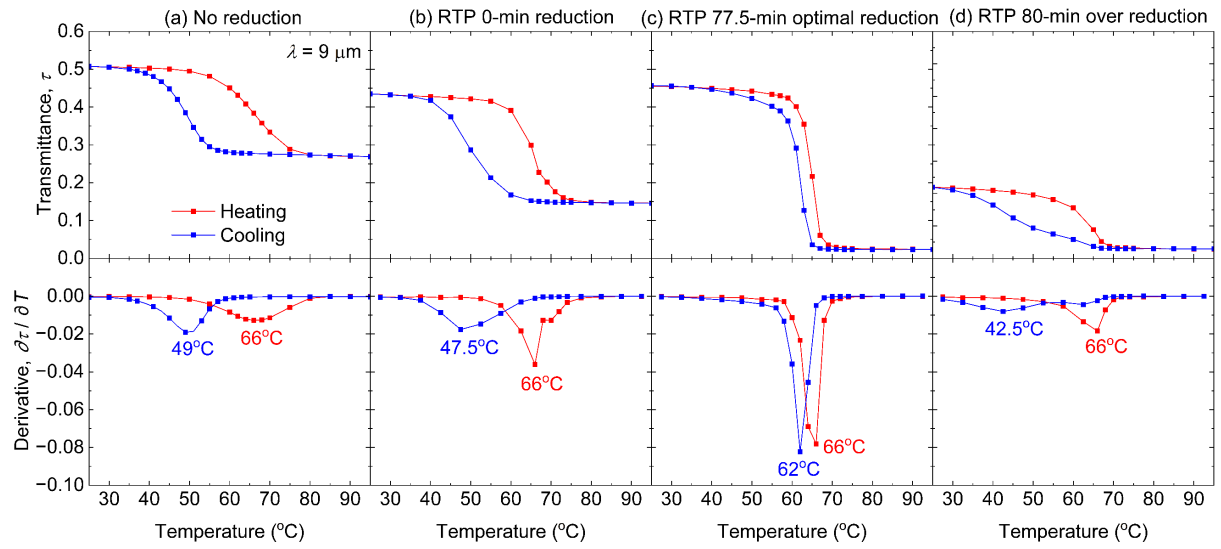


Figure 6. Insulator-to-metal phase transition behaviors of 150-nm vanadium thin film on undoped silicon wafer after (a) no reduction, (b) slight reduction (RTP 0 min), (c) optimal reduction (RTP 77.5 mins), (d) over reduction (RTP 80 mins): transmittance at $\lambda = 9 \mu\text{m}$ (top panel) and its derivative (bottom panel) with respect to temperature from both heating and cooling.

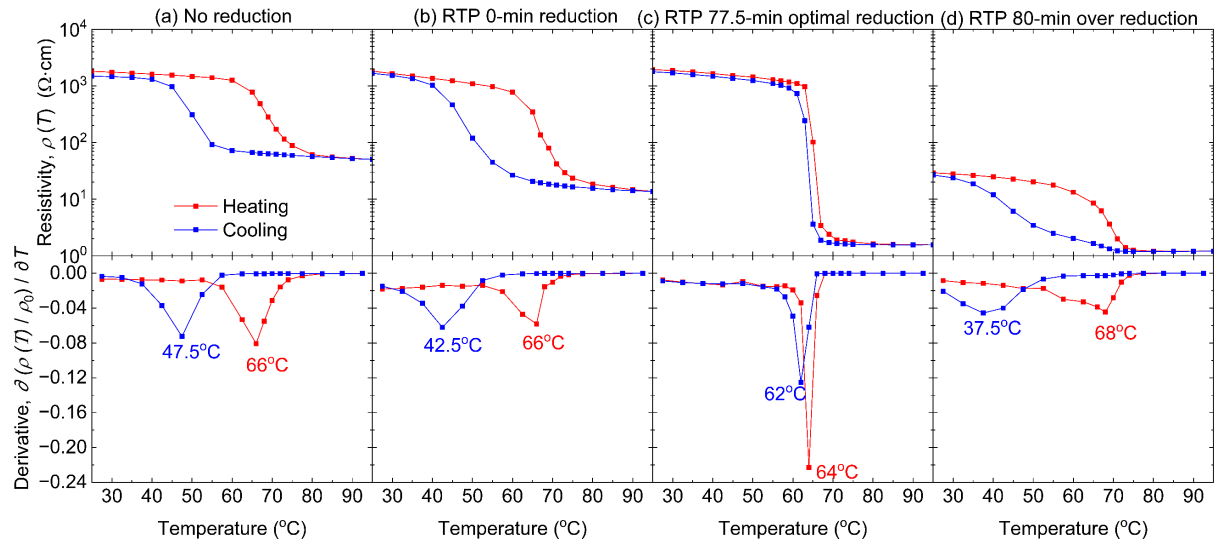


Figure 7. Temperature-dependent electrical resistivity (top panel) upon heating and cooling and its derivative with respect to temperature (bottom panel) of 150-nm vanadium thin film on undoped silicon wafer after (a) no reduction, (b) slight reduction (RTP 0 min), (c) optimal reduction (RTP 77.5 mins), (d) over reduction (RTP 80 mins), normalized to those measured at 25°C.

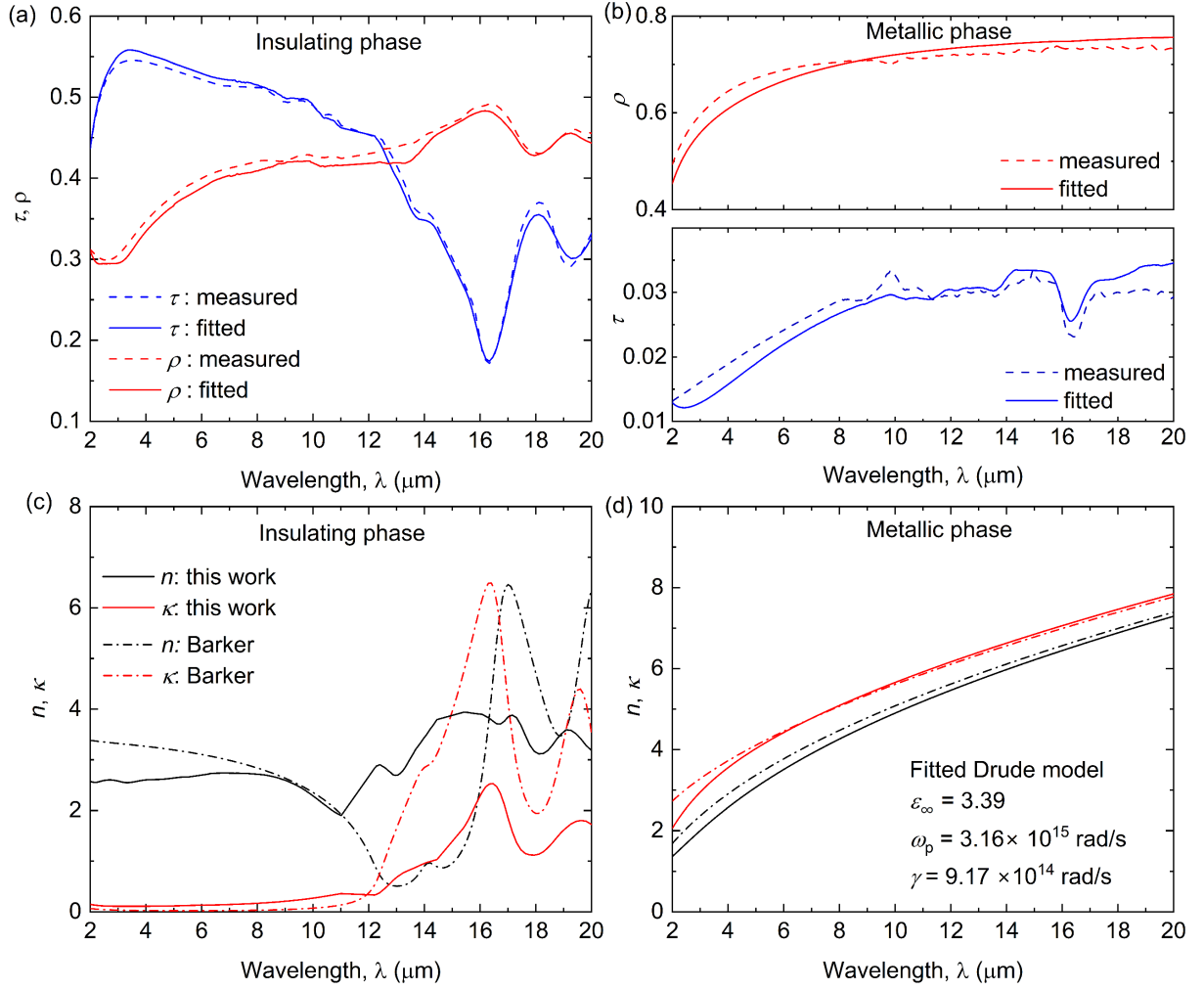


Figure 8. Modelled infrared transmittance (τ) and reflectance (ρ) spectra of optimal thermally grown 300 nm VO₂ thin film on undoped silicon wafer in comparison with FTIR measurements at (a) insulating phase (25°C) and (b) metallic phase (95°C). Fitted refractive index (n) and extinction coefficient (κ) at (c) insulating phase and (d) metallic phase with the data for single crystalline VO₂ from Barker et al. in Ref. [56] for comparison.